iScience

CellPress
OPEN ACCESS

Article

All-polymer indoor photovoltaic modules

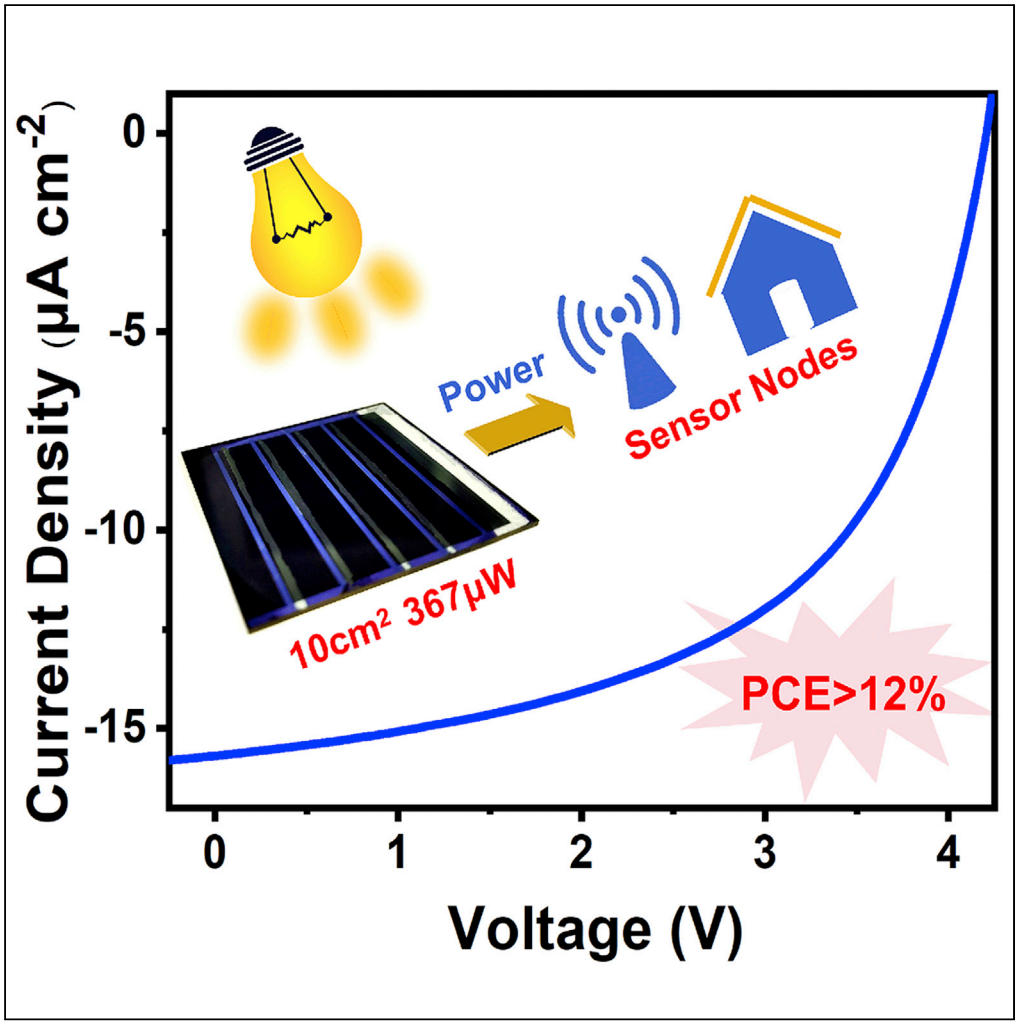

Yingze Zhang, Ning Wang, Yinghui Wang, Jidong Zhang, Jun Liu, Lixiang Wang

liujun@ciac.ac.cn

Highlights

The first all-polymer IPV module with the active area of 10 cm^2 was fabricated

The modules were processed with eco-friendly solvent and blade-coating methods

The modules exhibit the PCE of 12.04% and the power output of 367.2 μW at 1000 lux

Zhang et al., iScience *24*, 103104
October 22, 2021 © 2021
https://doi.org/10.1016/j.isci.2021.103104

iScience

CellPress
OPEN ACCESS

Article

All-polymer indoor photovoltaic modules

Yingze Zhang,[1,2] Ning Wang,[1,2] Yinghui Wang,[1,2] Jidong Zhang,[1] Jun Liu,[1,2,3,*] and Lixiang Wang[1,2]

SUMMARY

Indoor photovoltaic (IPV) with power output over 100 μW is promising to power the numerous sensor nodes in the Internet of Things (IoT) ecosystem. All polymer photovoltaic has the advantages of excellent thermal stability and superior mechanical properties. In this work, we fabricate the first all-polymer indoor photovoltaic module with the active area of 10 cm^2. The module uses polymer donor CD1 and new polymer acceptor PBN-21 with medium optical band gap of 1.9 eV as the active layer. It is processed with eco-friendly solvent tetrahydrofuran and the morphology can be improved by blade coating at 55°C. Under light emitting diode illumination at 1000 lux, the module exhibits a power conversion efficiency of 12.04% and a power output of 367.2 μW. The sufficient power output, high efficiency, excellent stability, and eco-friendly processing indicate that all-polymer indoor photovoltaic is a promising approach to achieve the self-powered of sensor nodes in the IoT ecosystem.

INTRODUCTION

Indoor photovoltaic (IPV) is attracting considerable attention because of the rapid development of Internet of Things (IoT) ecosystem, in which numerous sensor nodes collect and communicate data (Bai et al., 2021; Mathews et al., 2019; Cui et al., 2019a; Saeed et al., 2021). The power consumption of these sensor nodes is on the microwatt to milliwatt scale (Russo et al., 2017; Xie et al., 2021b; Arai et al., 2019a). To realize wireless and battery-free self-powered sensor nodes for practical applications, IPV is an attractive option because it harvests light energy from ambient conditions and generates electricity with high power output. Among the various IPV technologies, organic photovoltaic is most suitable because of its advantages of solution processing, flexibility, and the adjustable absorption spectra (Song et al., 2020; Zhu et al., 2021; Luke et al., 2021; Ma et al., 2021b; Cui et al., 2020a). In the past several years, great progress has been made in organic IPV. Its power conversion efficiency (PCE) has been enhanced to exceeding 30%, and the device operation lifetime exceeding 1000 h has also been demonstrated (Ma et al., 2020; Liao et al., 2020; Zhang et al., 2020).

All-polymer solar cells (all-PSCs), in which blends of polymer electron donors and polymer electron acceptors are used as active layers, have been regarded as a promising photovoltaic technology (Feng et al., 2020; Su et al., 2021; Zhao et al., 2020a; Jia et al., 2021; Sun et al., 2020). Compared with other photovoltaic technologies, all-PSCs have the unique merits of superior mechanical property and excellent morphological stability (Fan et al., 2020b; Zhang et al., 2018a; Xu et al., 2019a). In 2019, Liu et al. introduced all-polymer photovoltaic devices for IPV application, which show high open-circuit voltage (V_{OC}) and high PCE (Ding et al., 2019). Because the power requirement of sensor nodes in the IoT ecosystem is hundred milliwatt-class (Cui et al., 2020b), IPV with active area of ca. 10 cm^2 is adequate to power these sensor nodes when operated under typical indoor lighting conditions. This motivates us to develop all-polymer indoor photovoltaic (AP-IPV) modules.

To develop all-polymer photovoltaic modules, several challenges need to be overcome, including material design, processing solvent selection, and processing method. Firstly, a polymer donor and a polymer acceptor with medium band gap and suitable LUMO/HOMO energy level alignment should be developed or selected. Most of the existing polymer acceptors are designed for solar cell application. They have narrow bandgap and wide spectra to effectively absorb the visible light and infrared light under solar irradiation (Gao et al., 2016; Liu et al., 2021a; Wang et al., 2018). In comparison, lighting sources in IPV emit exclusively visible light and require polymer acceptors to have medium bandgap with proper energy level alignment (Li et al., 2020a, Li et al., 2020b; Cui et al., 2019b; Freunek et al., 2013; Zhao et al., 2020b). Secondly, the active layers should be processed with eco-friendly solvent without solvent additives.

[1]State Key Laboratory of Polymer Physics and Chemistry, Changchun Institute of Applied Chemistry, Chinese Academy of Sciences, Changchun 130022, P. R. China

[2]University of Science and Technology of China, Hefei 230026, P. R. China

[3]Lead contact

*Correspondence: liujun@ciac.ac.cn

https://doi.org/10.1016/j.isci.2021.103104

All-polymer active layers are usually processed with halogenated solvent, such as chloroform and chlorobenzene, which is harmful to the environment and human health and cannot be used for large-scale production (Wang et al., 2021; Xie et al., 2021a; Arai et al., 2019b). In addition, high-boiling-point solvent additives are always used to optimize phase separation morphology of the all-polymer active layers (Li et al., 2020a; Wang et al., 2019a; Lee et al., 2019). These solvent additives are difficult to be completely removed and are detrimental to device stability. Therefore, in view of the mass production of stable AP-IPV modules, active layers should be processed with non-halogenated and non-aromatic solvent without solvent additive. Thirdly, all polymer active layers should be processed with scalable fabrication techniques. It is well-known that phase separation morphology of active layer is very important for device performance (Liu et al., 2021b; Li et al., 2019; Zhang et al., 2021; Zhu et al., 2020; Ma et al., 2021a).

Small-area devices (<1 cm^2) are usually prepared by spin-coating, which cannot be used in large-area devices. Blade-coating can be used to fabricate large area devices and is compatible with the industrial roll-to-roll processing technique (Xiao et al., 2021; Zhao et al., 2018; Wang et al., 2019b). However, as the film-forming kinetics in blade-coating is totally different from that in spin-coating, the active layer morphology with blade-coating need to be carefully optimized for excellent photovoltaic performance (Zhang et al., 2018b; Wang et al., 2020; Yu et al., 2020).

In this work, for the first time, we report an efficient all-polymer indoor photovoltaic module. We at first develop a polymer donor and a polymer acceptor with medium bandgap of ca. 1.9 eV, and then we fabricate an all-polymer photovoltaic module with an active area of 10 cm^2 by blade coating with eco-friendly tetrahydrofuran (THF) as the processing solvent. The module shows a PCE of 12% as well as excellent thermal stability and photo stability in IPV application. Under light emitting diode (LED) illumination with the brightness of 1000 lux, the module affords an output power (P_{out}) of 367.2 μW, which can fulfill the power supply requirement of sensor nodes. This work represents a great progress toward the practical application of all-polymer photovoltaic.

RESULTS AND DISCUSSION

Materials

Figure 1C shows the chemical structures of the polymer donor CD1 and the polymer acceptor PBN-21 used in this work. CD1 is a polymer donor with medium optical band gap 1.95 eV. It is a D-A type polymer based on benzotriazole, and BTA-based polymer has realized the highest PCE over 14% (Zhou et al., 2021a, Zhou et al., 2021b). Moreover, this kind of BTA-based polymer can also be used in indoor OPV (Liu et al., 2020). The similar structure of CD1 is firstly reported by Li and co-workers (Bin et al., 2016). We followed the literature method and prepared CD1 with the number-average molecular weight (Mn) of 25.0 kDa and polydispersity index (PDI) of 1.92. PBN-21 is a polymer acceptor containing boron-nitrogen coordination bond (B←N) and is a derivative of our previously reported polymer acceptor PBN-10 (Wang et al., 2019c). The previous work demonstrated that polymer doner CD1 adopts face-on orientation in the active layers, whereas the polymer acceptor PBN-10 exhibits edge-on orientation. The mismatch between donor and acceptor orientation is not conducive to exciton dissociation (Wang et al., 2019c). Therefore, we adjusted the orientation of PBN-10 by ternary random copolymerization. PBN-21 is a random copolymer composed of double B←N bridged bipyridine (BNBP) unit, 1,4-dithienyl-2,3,5,6-tetrafluorobenzene unit and 1,4-dithiophene-2,5-difluorobenzene unit. PBN-21 was prepared by Stille polymerization of BNBP di-bromo monomer, 1,4-dithienyl-2,3,5,6-tetrafluorobenzene di-trimethyltin monomer and 1,4-dithiophene-2,5-difluorobenzene di-trimethyltin monomer. The synthetic route and synthesis procedures of PBN-21 can be found in the Supporting Information (see Figures S1 and S2 and Scheme S1). The Mn and PDI of PBN-21 are 68.5 kDa and 1.87, respectively. As a random copolymer, PBN-21 exhibits excellent solubility in common organic solvents, such as chlorobenzene, chloroform, THF, toluene, etc. This property makes PBN-21 processable with eco-friendly solvent, e.g., THF, which is non-aromatic and non-halogenated. The excellent solubility of CD1 and PBN-21 enable environmental-friendly solvent processing of photovoltaic devices (vide infra).

Optoelectronic properties

As shown in Figure 1D, the lowest unoccupied molecular orbital (LUMO) and the highest occupied molecular orbital (HOMO) energy levels of CD1 and PBN-21 are −2.91 eV/-5.28 eV and −3.48 eV/-5.91 eV, respectively. This energy level alignment would ensure photoinduced charge separation and lead to high V_{OC} in photovoltaic devices. Figure 1E shows the absorption spectra of CD1 and PBN-21, which are located in the

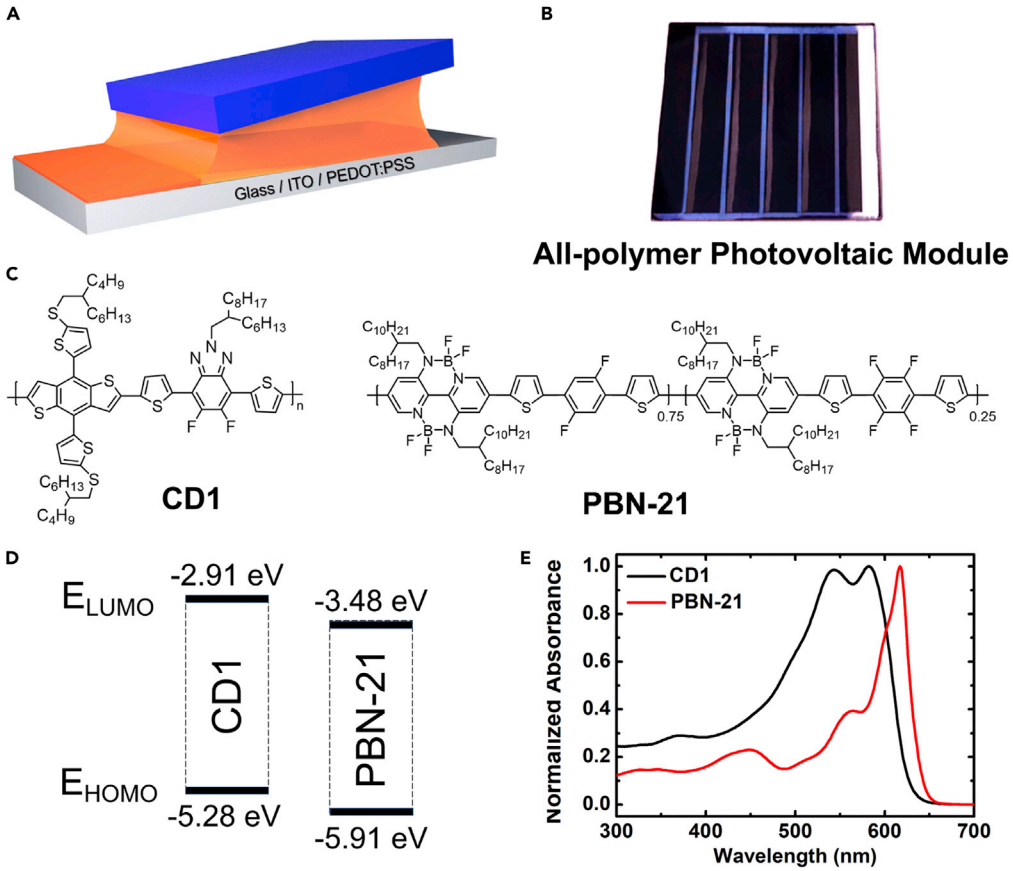

Figure 1. Module preparation process, molecular structure and physical properties

(A) Schematic illustration of blade coating method.

(B) Photo image of the all-polymer photovoltaic module.

(C) Chemical structures of CD1 and PBN-21.

(D) Energy level diagram of CD1 and PBN-21.

(E) Absorption spectra in thin film of CD1 and PBN-21.

visible region. Their absorption spectra overlap well with the emission spectra of indoor artificial light sources, suggesting strong indoor light harvesting capability (see Figures S3 and S4). Moreover, CD1 shows weak temperature-dependent aggregation (TDA) properties, while PBN-21 exhibits noticeable TDA properties in THF solution. As the solution temperature increases, the aggregation of PBN-21 is significantly weakened, which indicates that the aggregation behavior in the blend films can be adjusted by temperature. According to the onset absorption wavelength, the optical bandgap of CD1 and PBN-21 are determined to be 1.95 eV and 1.93 eV, respectively. These values are very close to the ideal band gaps of indoor photovoltaic materials of 1.9–2.0 eV (Venkateswararao et al., 2020; Ryu et al., 2020). All these results suggest that the opto-electronic properties of CD1 and PBN-21 are very suitable for IPV application.

Small area devices

Spin-coating is the widely used method to fabricate small-area organic photovoltaic devices. However, spin-coating cannot be used to fabricate large-area thin film. In this work, we adopt blade-coating to make all-polymer photovoltaic modules. Figure 1A shows the schematic illustration of blade-coating. Processing method plays an important role in phase separation morphology of active layers and consequently in photovoltaic performance of all polymer photovoltaic devices. Therefore, at first, using all-polymer photovoltaic devices with a small active area of 0.08 cm^2, we studied the effect of the processing method on the device performance of CD1:PBN-21. The device structure was ITO/PEDOT:PSS/active layer/LiF/Al. We selected THF as the processing solvent for environment-friendly processing. No solvent

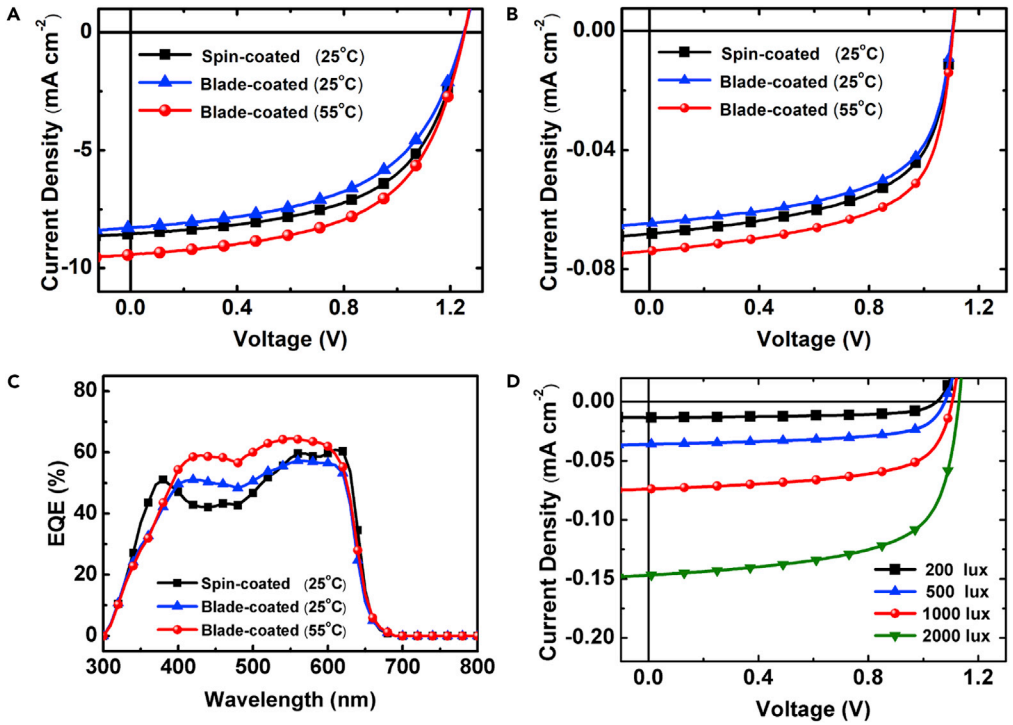

Figure 2. Photovoltaic properties of small-area devices

(A) *J-V* curves of the devices under AM 1.5G solar irradiation.

(B) *J-V* curves of the devices under 1000 Lux LED condition.

(C) EQE spectra of the spin-coated and blade-coated devices.

(D) *J-V* curves of the device blade-coated at 55°C under different light intensity.

additive was used because the solvent additive was difficult to be completely removed after the film-forming process and was detrimental to device stability. The weight ratio of CD1 and PBN-21 was 1:1 and the total concentration was 8 mg/mL. The active layers were prepared with the THF solution by spin-coated at 25°C, blade-coated at 25°C and blade-coated at 55°C.

Figure 2A shows the current density-voltage (*J-V*) curves of the three devices under AM 1.5G simulated solar light irradiation. The detailed parameters and specific optimization process are listed in Tables 1 and S1 and Figure S5. The spin-coated device shows a PCE of 6.10% with a V_{OC} of 1.25 V, a short-circuit current density (J_{SC}) of 8.56 mA cm^{-2}, and a fill factor (FF) of 57.0%. In comparison, the device blade-coated at 25°C exhibits a PCE of 5.59% with a V_{OC} of 1.25 V, a J_{SC} of 8.31 mA cm^{-2}, and an FF of 53.8%. The blade-coated device exhibits inferior photovoltaic performance to that of the spin-coated device. This is because of the poorer phase separation morphology of the blade-coated device (vide infra) because the prolonged film-forming process of blade-coating leads to large phase domain size. Therefore, we increase the temperature of the substrate in the blade-coating process to accelerate the film-forming process for optimal phase separation morphology. At the optimal substrate temperature of 55°C, the blade coated device gives a V_{OC} of 1.25 V, a J_{SC} of 9.43 mA cm^{-2}, and an FF of 57.8%, contributing to a PCE of 6.82%. This performance is even better than that of the spin-coated device. These results prove that all-polymer photovoltaic devices can give excellent performance when processed with blade coating and environment-friendly solvent.

Active layer morphology

The active layer morphology of the three devices was characterized by atomic force microscope (AFM), transmission electron microscope (TEM), and two-dimension grazing-incidence wide-angle X-ray scattering (2D-GIWAXS). The AFM and TEM images are shown in Figure 3. The two blade-coated films exhibit more obvious fibrous morphology than the spin-coated film. The root-mean-square roughness (R_q) of the

Table 1. Characteristics of the three all-polymer photovoltaic devices with the active area of 0.08 cm^2

Method	Irradiation	V_{OC} [V]	J_{SC} (J_{cal})[a] [mA cm^{-2}]	FF[%]	PCE (PCE_a)[b] [%]	P_{out} [mW cm^{-2}]	P_{in} [mW cm^{-2}]
spin-coated, 25°C	AM 1.5G	1.25	8.56 (8.42)	57.0	6.10 (5.93 ± 0.17)	6.10	100
	1000 lux	1.10	0.0681 (0.0668)	61.7	15.18 (14.95 ± 0.23)	0.0463	0.305
blade-coated, 25°C	AM 1.5G	1.25	8.31 (8.35)	53.8	5.59 (5.44 ± 0.15)	5.59	100
	1000 lux	1.10	0.0647 (0.0631)	60.1	14.03 (13.85 ± 0.18)	0.0428	0.305
blade-coated, 55°C	AM 1.5G	1.25	9.43 (9.42)	57.8	6.82 (6.65 ± 0.17)	6.82	100
	1000 lux	1.10	0.0739 (0.0706)	62.8	16.75 (16.56 ± 0.19)	0.0511	0.305

[a]J_{cal} is calculated by the EQE curve.
[b]The average Values PCE_a are calculated from 8 devices.

film blade-coated at 25°C is much larger than that of the film spin-coated at 25°C, suggesting larger phase separation size. This is due to the prolonged film-forming process in the former case because the solvent evaporates slower during blade-coating than during spin-coating. The film blade-coated at 55°C shows finer fibrous structure than that of the film blade-coated at 25°C, which can be attributed to the TDA properties of PBN-21. With the increase of solution temperature, the aggregation of PBN-21 is weakened, and the phase separation size of the blended film is reduced. This is consistent with the enhanced J_{SC} and PCE values in the former case than in the latter case.

Figures S13 and S14 show the 2D-GIWAXS patterns and the corresponding line cuts of pure films and the three blend films. The corresponding parameters are summarized in Tables S9 and S10. All the three active layers exhibit (100) peak at 0.24 $Å^{-1}$in the in-plane direction and (010) peak at 1.72 $Å^{-1}$ in the out-of-plane direction, suggesting that both CD1 and PBN-21 adopt face-on orientation in the active layers. We estimate the crystalline domain size of the active layer by calculating the coherence length (CL) with the Scherrer equation. The CL values of the (100) peaks for the active layers spin-coated at 25 °C, blade-coated at 25 °C, and blade-coated at 55 °C are 82 Å, 123 Å and 111 Å, respectively. The CL values of the (010) peaks for the three active layers are 30 Å, 38 Å and 36 Å, respectively. Compared with the spin-coated films, the blade-coated films show larger CL values, indicating that blade-coating can enhance crystallization of the polymers in the active layers. The film blade-coated at 55 °C shows smaller CL values than those of the film blade coated at 25 °C. This is probably due to the shortened film-forming process at increased blade-coating temperature. The AFM, TEM, and XRD results indicate that improved active layer morphology of polymer donor/polymer acceptor blends can be achieved after optimization of the blade-coating condition.

Charge transporting and recombination

The charge transporting behaviors of the three devices were characterized by space-charge limited current (SCLC) method with the *J–V* plots in dark of the hole-only and the electron-only devices. The results are shown in Figures S11 and S12, Tables S7 and S8. The devices spin-coated at 25°C, blade-coated at 25°C, and blade-coated at 55°C display μ_h values of 1.98 × 10^{-4}, 6.61 × 10^{-4}, and 4.46 × 10^{-4} cm^2 V^{-1} s^{-1} and μ_e values of 5.81 × 10^{-5}, 2.31 × 10^{-4}, and 2.77 × 10^{-4} cm^2 V^{-1} s^{-1}, respectively. The μ_h/μ_e ratios of the three devices are 3.40, 2.86, and 1.61, respectively. The two blade-coated devices exhibit higher μ_h and μ_e values than those of the spin-coated devices. This is probably due to the prolonged film-forming process of blade-coating, which leads to enhanced crystallinity of the polymers. In addition, the shearing force of blade-coating may also induce orientation of polymer chains and may contribute to the enhanced charge carrier mobilities. The device blade-coated at 55°C shows high and balanced electron and hole mobilities, which improve the charge sweeping out and contribute to the enhanced J_{SC} and FF.

We studied the charge extraction and recombination behaviors of the three devices by the dependence of effective voltage (V_{eff}) on photocurrent (J_{ph}) and the dependence of J_{SC} on light intensity (I). As shown in Figure S7A, all the three devices exhibit high and comparable charge collection efficiency. The

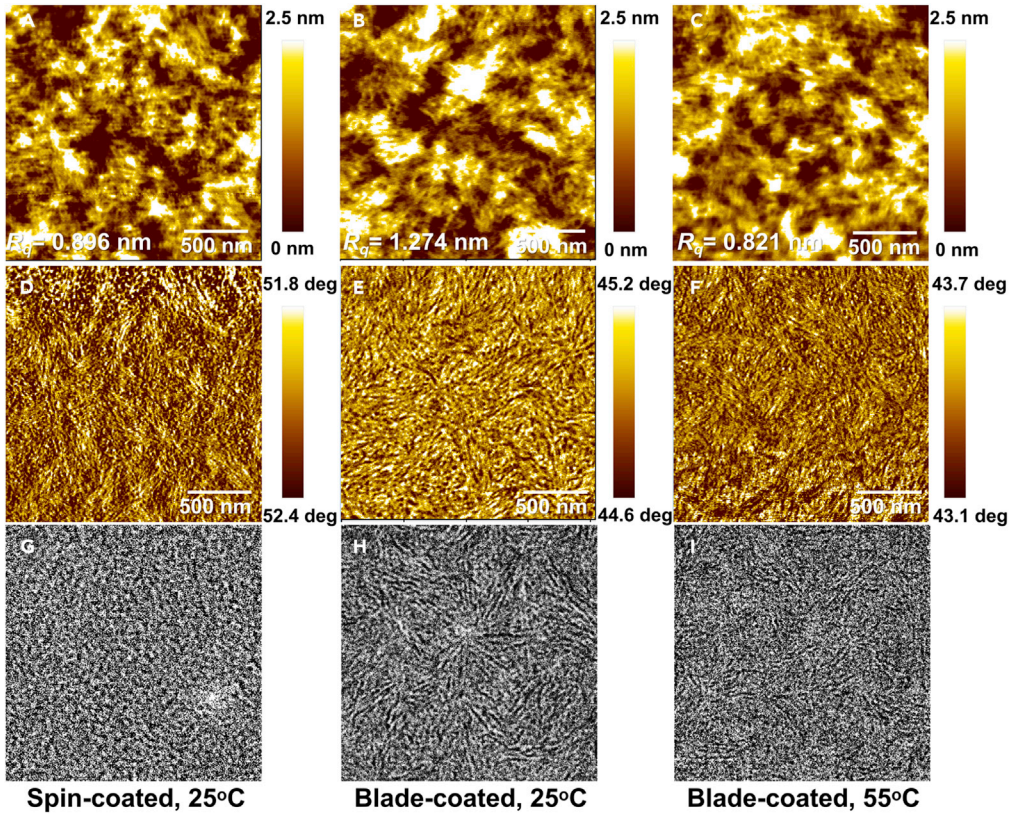

Figure 3. The morphology of the active layers of the three devices

(A–C) AFM height images.

(D–F) AFM phase images.

(G–I) TEM images. The scale bars of TEM images are the same as the AFM images.

dependence of J_{SC} on I of the three devices is displayed in Figure S7B. The relationship between J_{SC} and I is defined as $J_{SC} \propto I^{\alpha}$, and the α value can be used to evaluate the bimolecular recombination behavior of the devices. The α value close to 1 represents that all the free carriers can be swept out and collected by the electrodes without bimolecular charge recombination (Chai et al., 2020; Liu et al., 2018). The α values of the devices spin-coated at 25°C, blade-coated at 25°C, and blade-coated at 55°C are 0.933, 0.922 and 0.942, respectively. These results suggest that the device blade-coated at 55°C shows the weakest bimolecular charge recombination, which is in accordance with its excellent photovoltaic performance.

Indoor photovoltaics

As shown in Figure 2C, the external quantum efficiency (EQE) spectra of the three devices all locate in the visible region, indicating that they are suitable for IPV application. Figure 2B shows the *J-V* curves of the three devices under LED illumination at the brightness of 1000 lux. The device spin coated at 25°C exhibits a PCE of 15.18%, with a V_{OC} of 1.10 V, a J_{SC} of 68.1 μA cm^{-2}, and an FF of 61.7%. In comparison, the device blade coated at 55°C shows a V_{OC} of 1.10 V, a J_{SC} of 73.9 μA cm^{-2} and an FF of 62.8%, leading to a PCE of 16.75%. The light intensity of IPV is much lower than that of solar light irradiation. The *J-V* curves and detailed parameters of the optimal devices under different indoor light intensity are shown in Figures 2D and Table S2, the PCE of devices under 200 lux, 500 lux, and 2000 lux are 14.13%, 15.78% and 17.47%, respectively. As a result, the devices show decreased V_{OC} by 0.15 V and increased FF under indoor light illumination. Standard testing method of IPV is still a controversial subject because the estimation of real and exact light intensity can be affected by several factors. We calculate the J_{SC} values of the three devices by integrating their EQE curves and the LED emission spectrum together with the 1000 lux brightness. The results are shown in Table 1 and Figure S6. The calculated J_{SC} values are very comparable with the J_{SC} values obtained in our J-V scan, indicating that our indoor device performance results are reliable. We

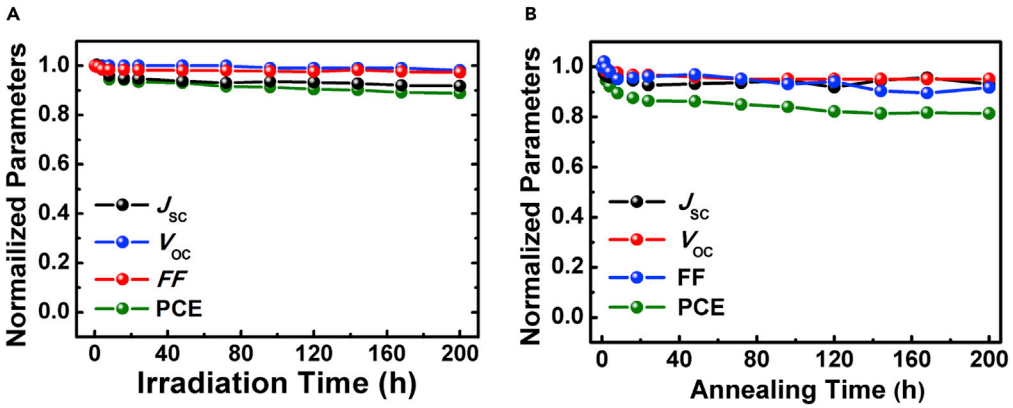

Figure 4. The stability of the all-polymer photovoltaic device

(A) Photovoltaic parameters of devices annealed at 120°C for 200 h.

(B) Photovoltaic parameters of devices illuminated at 1000 lux for 200 h.

also measured the photovoltaic performance of the device blade coated at 55°C under various light intensities (see Figure 2D). Under the light intensity of 500 lux, 1000 lux and 2000 lux, the PCE of the device is 15.78%, 16.75% and 17.47%, respectively.

Thermal and photo stability

It has been always reported that all-polymer photovoltaic devices exhibit excellent active layer morphology stability because the polymer chains entangle together in thin film (Xu et al., 2019b; Fan et al., 2020a; Kim et al., 2017). In this work, we also find that the CD1:PBN-21-based devices show excellent thermal stability and photostability (see Figures S9 and S10, Tables S5 and S6). The device stability measurement was carried out in a nitrogen-filled glove box without device encapsulation. To investigate the thermal stability, the CD1:PBN-21-based device was thermal annealed at 120°C for 200 h and the device photovoltaic characteristics were monitored. As shown in Figure 4A, the all-polymer photovoltaic device keeps 82% of its PCE after thermal annealing at 120°C for 200 h, suggesting excellent thermal stability. After 1000 lux LED illumination for 200 h, the all-polymer photovoltaic device shows only 10% decrease of its PCE, indicating superior photo stability. The excellent stability together with the high photovoltaic efficiency indicates that all-polymer photovoltaic is competitive for practical IPV application.

All-polymer photovoltaic module

Considering the power requirement of sensor nodes, we fabricated all polymer photovoltaic modules with the effective area of 10 cm^2. The module was made on a 5 cm × 5 cm glass substrate with the geometric FF of 40%. As shown in Figure 5A, the module consists of five cells connected in series, and each cell has the size of 4.6 cm × 0.44 cm. The photo image of the module is shown in Figure 1B. The active layer of the module was deposited by blade coating at 55°C with the THF solution of CD1 and PBN-21. To our best knowledge, this is the first report of an all-polymer photovoltaic module for IPV application. The *J-V* curves of the module under AM 1.5G solar irradiation and 1000 lux LED condition are displayed in Figures 5C and 5D, respectively. The device parameters are listed in Table 2. Under AM 1.5G solar light irradiation, the module exhibits a PCE of 5.18% with a V_{OC} of 5.94 V, a J_{SC} of 1.76 mA cm^{-2}, and an FF of 49.7%. Under 1000 lux LED illumination, the module shows a PCE of 12.04% with a V_{OC} of 4.20 V, a J_{SC} of 15.7 μA cm^{-2}, and an FF of 55.7%. The *J-V* curves and detailed parameters of the module under different indoor light intensity are shown in Figure 5D and Table S3, the PCE of devices under 200 lux, 500 lux and, 2000 lux are 10.83%,

Table 2. Characteristics of the all-polymer photovoltaic module

Irradiation source	V_{OC} [V]	J_{SC} [mA cm^{-2}]	FF [%]	PCE (PCE$_a$)[a][%]	P_{out} [mW cm^{-2}]	P_{in} [mW cm^{-2}]
AM 1.5G	5.94	1.76	49.7	5.18 (5.06 ± 0.12)	5.18	100
1000 lux	4.20	0.0157	55.7	12.04 (11.88 ± 0.16)	0.0367	0.305

[a]The average Values PCE$_a$ are calculated from 8 devices.

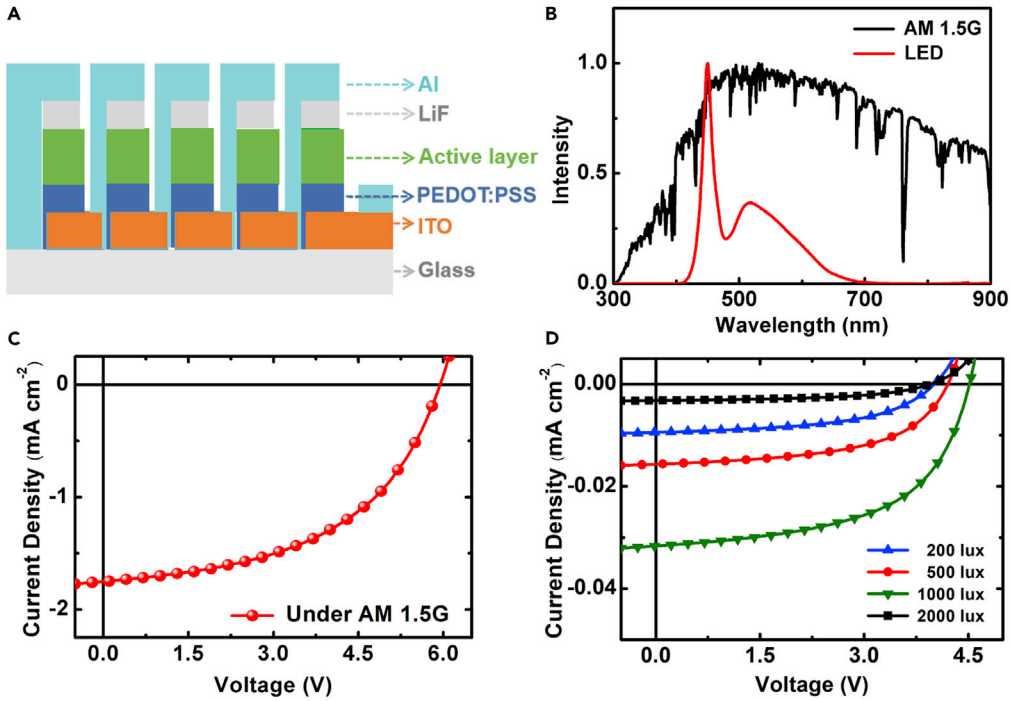

Figure 5. Structure and photovoltaic properties of all-polymer photovoltaic module

(A) Structure of the photovoltaic module, in which five single cells are connected in series.

(B) Emission Spectra of the LED lighting source and the solar spectrum.

(C) *J-V* curves of modules under AM 1.5G solar irradiation.

(D) *J-V* curves of modules under indoor LED illumination.

11.62%, and 13.01%, respectively. Compared to the 0.08 cm^2 devices, the module exhibits only 24% loss in PCE. Under indoor conditions, the module provides a power generation of 367 μW at the voltage of 4.2 V, which is sufficient to power sensor nodes or other wireless electronic devices.

Conclusions

In summary, we have demonstrated an all-polymer indoor photovoltaic module using the blend of a polymer donor and a polymer acceptor with medium optical bandgap as the active layer. The module is fabricated by blade coating at elevated temperature with eco-friendly THF as the solvent. Under LED illumination at the brightness of 1000 lux, the all-polymer photovoltaic module exhibits a PCE of 12.04% and a power output of 367.2 μW, which meets the power supply requirements of sensor nodes in IoT. Moreover, excellent photo stability and thermal stability have also been demonstrated with the small area all-polymer photovoltaic devices. These results indicate that all-polymer indoor photovoltaics are promising to power wireless self-powered sensor nodes in the IoT ecosystem.

Limitations of the study

There are many other efficient all-polymer active layers which can be applied to AP-IPV modules. AP-IPV modules with higher PCE and higher power output can be explored.

STAR★METHODS

Detailed methods are provided in the online version of this paper and include the following:

- KEY RESOURCE TABLE
- RESOURCE AVAILABILITY
  - Lead contact
  - Materials availability
  - Data and code availability

SUPPLEMENTAL INFORMATION

Supplemental information can be found online at https://doi.org/10.1016/j.isci.2021.103104.

ACKNOWLEDGMENTS

This work was supported by the National Key Research and Development Program of China (No. 2019YFA0705902) funded by MOST and the National Natural Science Foundation of China (No. 21875244, 21625403).

AUTHOR CONTRIBUTIONS

Y.Z. performed the fabrication and characterization of all-polymer photovoltaic devices, including module design, *J-V* test, stability test, and morphology characterization. Y.Z. N.W. and J.L. conducted the data analysis. Y.W. synthesized PBN-21 and conducted ^{1}H NMR and thermogravimetric test. J.Z performed the 2D-GIWAXS characterization. The project was supervised and directed by J.L.. Y.Z. wrote the manuscript with large contributions from N.W., J.L., and L.W.. All authors commented on the manuscript for improvements.

DECLARATION OF INTERESTS

The authors declare no competing financial interest.

Received: June 29, 2021
Revised: August 3, 2021
Accepted: September 4, 2021
Published: October 22, 2021

REFERENCES

Arai, R., Furukawa, S., Sato, N., and Yasuda, T. (2019a). Organic energy-harvesting devices achieving power conversion efficiencies over 20% under ambient indoor lighting. J. Mater. Chem. A *7*, 20187–20192.

Arai, R., Furukawa, S., Hidaka, Y., Komiyama, H., and Yasuda, T. (2019b). High-performance organic energy-harvesting devices and modules for self-sustainable power generation under ambient indoor lighting environments. ACS Appl. Mater. Interfaces *11*, 9259–9264.

Bai, F., Zhang, J., Zeng, A., Zhao, H., Duan, K., Yu, H., Cheng, K., Chai, G., Chen, Y., Liang, J., et al. (2021). A highly crystalline non-fullerene acceptor enabling efficient indoor organic photovoltaics with high EQE and fill factor. Joule *5*, 1231–1245.

Bin, H., Zhang, Z.G., Gao, L., Chen, S., Zhong, L., Xue, L., Yang, C., and Li, Y. (2016). Non-Fullerene polymer solar cells based on alkylthio and fluorine substituted 2D-conjugated polymers reach 9.5% efficiency. J. Am. Chem. Soc. *138*, 4657–4664.

Chai, G., Zhang, J., Pan, M., Wang, Z., Yu, J., Liang, J., Yu, H., Chen, Y., Shang, A., Liu, X., et al. (2020). Deciphering the role of chalcogen-containing heterocycles in nonfullerene acceptors for organic solar cells. ACS Energy Lett. *5*, 3415–3425.

Cui, Y., Yao, H., Zhang, T., Hong, L., Gao, B., Xian, K., Qin, J., and Hou, J. (2019a). 1 cm^2 organic photovoltaic cells for indoor application with over 20% efficiency. Adv. Mater. *31*, e1904512.

Cui, Y., Wang, Y., Bergqvist, J., Yao, H., Xu, Y., Gao, B., Yang, C., Zhang, S., Inganäs, O., Gao, F., and Hou, J. (2019b). Wide-gap non-fullerene acceptor enabling high-performance organic photovoltaic cells for indoor applications. Nat. Energy *4*, 768–775.

Cui, Y., Yao, H., Hong, L., Zhang, T., Tang, Y., Lin, B., Xian, K., Gao, B., An, C., Bi, P., et al. (2020a). Organic photovoltaic cell with 17% efficiency and superior processability. Natl. Sci. Rev. *7*, 1239–1246.

Cui, Y., Hong, L., and Hou, J. (2020b). Organic photovoltaic cells for indoor applications: Opportunities and challenges. ACS Appl. Mater. Interfaces *12*, 38815–38828.

Ding, Z., Zhao, R., Yu, Y., and Liu, J. (2019). All-polymer indoor photovoltaics with high open-circuit voltage. J. Mater. Chem. A *7*, 26533–26539.

Dou, C., Long, X., Ding, Z., Xie, Z., Liu, J., and Wang, L. (2016). An electron-deficient building block based on the B←N unit: an electron acceptor for all-polymer solar cells. Angew. Chem. Int. Ed. *55*, 1436–1440.

Fan, Q., Su, W., Chen, S., Liu, T., Zhuang, W., Ma, R., Wen, X., Yin, Z., Luo, Z., Guo, X., et al. (2020a). A non-conjugated polymer acceptor for efficient and thermally stable All-polymer solar cells. Angew. Chem. Int. Ed. *59*, 19835.

Fan, Q., Su, W., Chen, S., Kim, W., Chen, X., Lee, B., Liu, T., Méndez-Romero, U.A., Ma, R., Yang, T., et al. (2020b). Mechanically robust all-polymer solar cells from narrow band gap acceptors with hetero-bridging atoms. Joule *4*, 658–672.

Feng, K., Huang, J., Zhang, X., Wu, Z., Shi, S., Thomsen, L., Tian, Y., Woo, H.Y., McNeill, C.R., and Guo, X. (2020). High-performance all-polymer solar cells enabled by n-type polymers with an ultranarrow bandgap down to 1.28 eV. Adv. Mater. *32*, e2001476.

Freunek, M., Freunek, M., and Reindl, L.M. (2013). Maximum efficiencies of indoor photovoltaic devices. IEEE J. Photovolt. *3*, 59.

Gao, L., Zhang, Z.G., Bin, H., Xue, L., Yang, Y., Wang, C., Liu, F., Russell, T.P., and Li, Y. (2016). High-efficiency nonfullerene polymer solar cells with medium bandgap polymer donor and narrow bandgap organic semiconductor acceptor. Adv. Mater. *28*, 8288–8295.

Jia, T., Zhang, J., Zhang, K., Tang, H., Dong, S., Tan, C.-H., Wang, X., and Huang, F. (2021). All-polymer solar cells with efficiency approaching 16% enabled using a dithieno[3′,2′:3,4;2″,3″:5,6]benzo[1,2-c][1,2,5]thiadiazole (fDTBT)-based polymer donor. J. Mater. Chem. A *9*, 8975–8983.

Kim, T., Choi, J., Kim, H.J., Lee, W., and Kim, B.J. (2017). Comparative study of thermal stability, morphology, and performance of all-polymer, fullerene–polymer, and ternary blend solar cells based on the same polymer donor. Macromolecules *50*, 6861–6871.

Lee, C., Lee, S., Kim, G.U., Lee, W., and Kim, B.J. (2019). Recent advances, design guidelines, and prospects of all-polymer solar cells. Chem. Rev. *119*, 8028–8086.

Li, Z., Zhong, W., Ying, L., Liu, F., Li, N., Huang, F., and Cao, Y. (2019). Morphology optimization via molecular weight tuning of donor polymer enables all-polymer solar cells with simultaneously improved performance and stability. Nano Energy *64*, 103931.

Li, M., Igbari, F., Wang, Z.K., and Liao, L.S. (2020a). Indoor thin-film photovoltaics: progress and challenges. Adv. Energy Mater. *10*, 2000641.

Li, Q., Wang, L.-M., Liu, S., Guo, L., Dong, S., Ma, G., Cao, Z., Zhan, X., Gu, X., Zhu, T., et al. (2020b). Vertical composition distribution and crystallinity regulations enable high-performance polymer solar cells with >17% efficiency. ACS Energy Lett. *5*, 3637–3646.

Liao, C.-Y., Chen, Y., Lee, C.-C., Wang, G., Teng, N.-W., Lee, C.-H., Li, W.-L., Chen, Y.-K., Li, C.-H., Ho, H.-L., et al. (2020). Processing strategies for an organic photovoltaic module with over 10% efficiency. Joule *4*, 189–206.

Liu, J., Ma, L.-K., Sheong, F.K., Zhang, L., Hu, H., Zhang, J.-X., Zhang, J., Li, Z., Ma, C., Han, X., et al. (2018). Carboxylate substitution position influencing polymer properties and enabling non-fullerene organic solar cells with high open circuit voltage and low voltage loss. J. Mater. Chem. A *6*, 16874–16881.

Liu, L., Zhang, H., Xiao, B., Liu, Y., Xu, B., Wang, C., Wen, S., Zhou, E., Chen, G., Im, C., and Tian, W. (2020). Effects of BTA2 as the third component on the charge carrier generation and recombination behavior of PTB7:PC71BM photovoltaic system. Front. Chem. Sci. Eng. *15*, 127–137.

Liu, W., Xu, X., Yuan, J., Leclerc, M., Zou, Y., and Li, Y. (2021a). Low-bandgap non-fullerene acceptors enabling high-performance organic solar cells. ACS Energy Lett. *6*, 598–608.

Liu, T., Yang, T., Ma, R., Zhan, L., Luo, Z., Zhang, G., Li, Y., Gao, K., Xiao, Y., Yu, J., et al. (2021b). 16% efficiency all-polymer organic solar cells enabled by a finely tuned morphology via the design of ternary blend. Joule *5*, 914–930.

Long, X., Ding, Z., Dou, C., Zhang, J., Liu, J., and Wang, L. (2016). Polymer acceptor based on double B←N bridged bipyridine (BNBP) unit for high-efficiency all-polymer solar cells. Adv. Mater. *28*, 6504–6508.

Long, X., Yao, J., Cheng, F., Dou, C., and Xia, Y. (2019). Double B←N bridged bipyridine-containing polymer acceptors with enhanced electron mobility for all-polymer solar cells. Mater. Chem. Front. *3*, 70–77.

Luke, J., Corrêa, L., Rodrigues, J., Martins, J., Daboczi, M., Bagnis, D., and Kim, J.S. (2021). A commercial benchmark: light-soaking free, fully scalable, large-area organic solar cells for low-light applications. Adv. Energy Mater. *11*, 2003405.

Ma, X., Zeng, A., Gao, J., Hu, Z., Xu, C., Son, J., Jeong, S., Zhang, C., Li, M., Wang, K., et al. (2021a). Approaching 18% effificiency of ternary organic photovoltaics with wide bandgap polymer donor and well compatible Y6 : Y6-1O as acceptor. Natl. Sci. Rev. *8*, nwaa305.

Ma, R., Tao, Y., Chen, Y., Liu, T., Luo, Z., Guo, Y., Xiao, Y., Fang, J., Zhang, G., Li, X., et al. (2021b). Achieving 16.68% efficiency ternary as-cast organic solar cells. Sci. China Chem. *64*, 581–589.

Ma, L.-K., Chen, Y., Chow, P.C.Y., Zhang, G., Huang, J., Ma, C., Zhang, J., Yin, H., Hong Cheung, A.M., Wong, K.S., et al. (2020). High-efficiency indoor organic photovoltaics with a band-aligned interlayer. Joule *4*, 1486–1500.

Mathews, I., Kantareddy, S.N., Buonassisi, T., and Peters, I.M. (2019). Technology and market perspective for indoor photovoltaic cells. Joule *3*, 1415–1426.

Rivnay, J., Mannsfeld, S., Miller, C., Salleo, A., and Toney, M. (2012). Quantitative determination of organic semiconductor microstructure from the molecular to device scale. Chem. Rev. *112*, 5488–5519.

Russo, J., Ray, W., and Litz, M.S. (2017). Low light illumination study on commercially available homojunction photovoltaic cells. Appl. Energy *191*, 10–21.

Ryu, H.S., Park, S.Y., Lee, T.H., Kim, J.Y., and Woo, H.Y. (2020). Recent progress in indoor organic photovoltaics. Nanoscale *12*, 5792–5804.

Saeed, M.A., Kim, S.H., Kim, H., Liang, J., Woo, H.Y., Kim, T.G., Yan, H., and Shim, J.W. (2021). Indoor organic photovoltaics: optimal cell design principles with synergistic parasitic resistance and optical modulation effect. Adv. Energy Mater. *11*, 2003103.

Song, J., Zhang, M., Yuan, M., Qian, Y., Sun, Y., and Liu, F. (2018). Morphology characterization of bulk heterojunction solar cells. Small Methods *2*, 1700229.

Song, W., Peng, R., Huang, L., Liu, C., Fanady, B., Lei, T., Hong, L., Ge, J., Facchetti, A., and Ge, Z. (2020). Over 14% efficiency folding-flexible ITO-free organic solar cells enabled by eco-friendly acid-processed electrodes. iScience *23*, 100981.

Su, N., Ma, R., Li, G., Liu, T., Feng, L.-W., Lin, C., Chen, J., Song, J., Xiao, Y., Qu, J., et al. (2021). High-efficiency all-polymer solar cells with poly-small-molecule acceptors having π-extended units with broad near-IR absorption. ACS Energy Lett. *6*, 728–738.

Sun, H., Liu, B., Yu, J., Zou, X., Zhang, G., Zhang, Y., Zhang, W., Su, M., Fan, Q., Yang, K., et al. (2020). Reducing energy loss via tuning energy levels of polymer acceptors for efficient all-polymer solar cells. Sci. China Chem. *63*, 1785–1792.

Venkateswararao, A., Ho, J.K.W., So, S.K., Liu, S.-W., and Wong, K.-T. (2020). Device characteristics and material developments of indoor photovoltaic devices. Mater. Sci. Eng. R Rep. *139*, 100517.

Wang, J., Xie, S., Zhang, D., Wang, R., Zheng, Z., Zhou, H., and Zhang, Y. (2018). Ultra-narrow bandgap non-fullerene organic solar cells with low voltage losses and a large photocurrent. J. Mater. Chem. A *6*, 19934–19940.

Wang, J., Gao, Y., Yu, Y., Zhao, R., Zhang, L., and Liu, J. (2021). All-polymer indoor photovoltaics based on polymer acceptors with various bandgap. Org. Electron. *92*, 106134.

Wang, G., Melkonyan, F.S., Facchetti, A., and Marks, T.J. (2019a). All-polymer solar cells: recent progress, challenges, and prospects. Angew. Chem. Int. Ed. *58*, 4129–4142.

Wang, G., Adil, M.A., Zhang, J., and Wei, Z. (2019b). Large-area organic solar cells: material requirements, modular designs, and printing methods. Adv. Mater. *31*, e1805089.

Wang, N., Long, X., Ding, Z., Feng, J., Lin, B., Ma, W., Dou, C., Liu, J., and Wang, L. (2019c). Improving active layer morphology of all-polymer solar cells by dissolving the two polymers individually. Macromolecules *52*, 2402–2410.

Wang, Y., Wang, X., Lin, B., Bi, Z., Zhou, X., Naveed, H.B., Zhou, K., Yan, H., Tang, Z., and Ma, W. (2020). Achieving balanced crystallization kinetics of donor and acceptor by sequential-blade coated double bulk heterojunction organic solar cells. Adv. Energy Mater. *10*, 2000826.

Xiao, Y., Zuo, C., Zhong, J.X., Wu, W.Q., Shen, L., and Ding, L. (2021). Large-area blade-coated solar cells: advances and perspectives. Adv. Energy Mater. *11*, 2100378.

Xie, L., Zhang, J., Song, W., Hong, L., Ge, J., Wen, P., Tang, B., Wu, T., Zhang, X., Li, Y., and Ge, Z. (2021a). Understanding the effect of sequential deposition processing for high-efficient organic photovoltaics to harvest sunlight and artificial light. ACS Appl. Mater. Interfaces *13*, 20405–20416.

Xie, L., Song, W., Ge, J., Tang, B., Zhang, X., Wu, T., and Ge, Z. (2021b). Recent progress of organic photovoltaics for indoor energy harvesting. Nano Energy *82*, 105770.

Xu, Y., Yuan, J., Zhou, S., Seifrid, M., Ying, L., Li, B., Huang, F., Bazan, G.C., and Ma, W. (2019a). Ambient processable and stable All-polymer organic solar cells. Adv. Funct. Mater. *29*, 1806747.

Xu, Y., Yuan, J., Liang, S., Chen, J.-D., Xia, Y., Larson, B.W., Wang, Y., Su, G.M., Zhang, Y., Cui, C., et al. (2019b). Simultaneously improved efficiency and stability in all-polymer solar cells by a P-i-N architecture. ACS Energy Lett. *4*, 2277–2286.

Yu, Y., Sun, R., Wang, T., Yuan, X., Wu, Y., Wu, Q., Shi, M., Yang, W., Jiao, X., and Min, J. (2020). Improving photovoltaic performance of non-fullerene polymer solar cells enables by fine-tuning blend microstructure via binary solvent mixtures. Adv. Funct. Mater. *31*, 2008767.

Zhang, Y., Duan, C., and Ding, L. (2020). Indoor organic photovoltaics. Sci. Bull. *65*, 2040–2042.

Zhang, Y., Xu, Y., Ford, M.J., Li, F., Sun, J., Ling, X., Wang, Y., Gu, J., Yuan, J., and Ma, W. (2018a). Thermally stable All-polymer solar cells with high tolerance on blend ratios. Adv. Energy Mater. *8*, 1800029.

Zhang, L., Xu, X., Lin, B., Zhao, H., Li, T., Xin, J., Bi, Z., Qiu, G., Guo, S., Zhou, K., et al. (2018b). Achieving balanced crystallinity of donor and acceptor by combining blade-coating and ternary strategies in organic solar cells. Adv. Mater. *30*, e1805041.

Zhang, D., Fan, P., Shi, J., Zheng, Y., Zhong, J., and Yu, J. (2021). Control of vertical phase separation in high performance non-fullerene organic solar cell by introducing oscillating stratification preprocessing. Nano Res. *14*, 1319–1325.

Zhao, R., Wang, N., Yu, Y., and Liu, J. (2020a). Organoboron polymer for 10% efficiency all-polymer solar cells. Chem. Mater. *32*, 1308–1314.

Zhao, R., Liu, J., and Wang, L. (2020b). Polymer acceptors containing B←N units for organic photovoltaics. Acc. Chem. Res. *53*, 1557–1567.

Zhao, W., Zhang, S., Zhang, Y., Li, S., Liu, X., He, C., Zheng, Z., and Hou, J. (2018). Environmentally friendly solvent-processed organic solar cells that are highly efficient and adaptable for the blade-coating method. Adv. Mater. *30*, 1704837.

Zhou, J., Cong, P., Chen, L., Zhang, B., Geng, Y., Tang, A., and Zhou, E. (2021a). Gradually modulating the three parts of D-p-A type polymers for high-performance organic solar cells. J. Energy Chem. *62*, 532–537.

Zhou, J., Zhang, B., Du, M., Dai, T., Tang, A., Guo, Q., and Zhou, E. (2021b). Side-chain engineering of copolymers based on benzotriazole (BTA) and dithieno[2,3-d;2′,3′-d′]benzo[1,2-b;4,5-b′] dithiophenes (DTBDT) enables a high PCE of 14.6%. Nanotechnology *32*, 225403.

Zhu, C., Li, Z., Zhong, W., Peng, F., Zeng, Z., Ying, L., Huang, F., and Cao, Y. (2021). Constructing a new polymer acceptor enabled non-halogenated solvent-processed all-polymer solar cell with an efficiency of 13.8. Chem. Commun. *57*, 935–938.

Zhu, W., Spencer, A.P., Mukherjee, S., Alzola, J.M., Sangwan, V.K., Amsterdam, S.H., Swick, S.M., Jones, L.O., Heiber, M.C., Herzing, A.A., et al. (2020). Crystallography, morphology, electronic structure, and transport in non-fullerene/non-indacenodithienothiophene polymer:Y6 solar cells. J. Am. Chem. Soc. *142*, 14532–14547.

STAR★METHODS

KEY RESOURCE TABLE

REAGENT or RESOURCE	SOURCE	IDENTIFIER
Chemicals, peptides, and recombinant proteins		
n-Hexane, AR	JDTZ Precision Chemical Reagent Factory	Q/12HG-989-2001
Acetine, AR	Shuang Fu Chemical Reagent	GR686-89
Isopropyl alcohol, AR	JDTZ Precision Chemical Reagent Factory	XK13-011-00009
Trichloromethane, AR	XILONG Scientific	XK13-011-00036
Toluene, AR	XILONG Scientific	GB/T684-1999
PEDOT:PSS	H. C. Starck Inc.	Clevios VP AI 4083
Critical commercial assays		
Fiber Optics Spectrometer	Ocean Optics	Maya2000 Pro
Transmission electron microscope	JEOL	JEM-1400
Atomic force microscope	Seiko Instruments	SPI 3800 controller
Other		
Solar Simulator	SAN-EI Electric Co., Ltd.	XES-40S2-CE
Solar Cell Spectral Response Measurement System	Enlitech Co., Ltd.	QE-R3011
General Purpose Digital Source Meter	Keithley	2400

RESOURCE AVAILABILITY

Lead contact

Further information and requests for resources and reagents should be directed to and will be fulfilled by the lead contact, Jun Liu (liujun@ciac.ac.cn)

Materials availability

The new polymer acceptor PBN-21 generated in this study will be made available on request, but we may require a payment and/or a completed Materials Transfer Agreement if there is potential for commercial application.

Data and code availability

This paper did not generate and does not report original code. The Critical assays and chemicals used in this study are described in the method details and key resource table. All data reported in this paper will be shared by the lead contact upon request. Any additional information required to reanalyze the data reported in this work paper is available from the Lead Contact upon the reasonable request.

EXPERIMENTAL MODEL AND SUBJECT DETAILS

No experimental model was used in this work. The specific experimental details are provided in method details.

METHOD DETAILS

Materials

Polymer CD1 was synthesized in our laboratory according our previous reported method (Zhao et al., 2020a). PBN-21 was synthesized with the synthetic route shown in Scheme S1. The three monomers were synthesized following the literature procedures (Dou et al., 2016; Long et al., 2016, 2019).

Synthesis of PBN-21

Under argon atmosphere, a mixture of double B←N bridged bipyridine (119.5 mg, 0.098 mmol), 2,2′ -(tetrafluoro-1,4-phenylene)dithiophene (15.6 mg, 0.024 mmol), 2,2′ -(2,5-difluoro-1,4-phenylene)dithiophene (44.2 mg, 0.072 mmol), $Pd(PPh_3)_4$ (1.1 mg, 0.001 mmol) and toluene (10 mL) was stirred at 120°C for 30 h. After cooled down, the reaction mixture was poured to methanol and the dark violet precipitate was collected. The solid was purified by sequential Soxhlet extraction with acetone, hexane and $CHCl_3$. The chloroform fraction was concentrated and then poured to methanol. The resulting dark violet precipitate was finally collected by filtration and dried in vacuum overnight. Yield: 120.1 mg (92%). ^{1}H NMR (400 MHz, $C_2D_2Cl_4$) δ (ppm) 8.37 (s, 1H), 7.68 (s, 1.3H), 7.52 (s, 2.7H), 3.56 (s, 2H), 1.84 (s, 1H), 1.49–1.10 (m, 55H), 0.79 (t, J = 6.4 Hz, 6H). Anal. Calcd.: C, 71.29; H, 9.05; N, 4.16; S, 4.76. Found: C, 71.06; H, 8.86; N, 3.95; S, 4.95.

Characterization

UV–vis absorption spectra of polymers in solution and in thin film were measured with a PerkinElmer Lambda 35 UV−vis spectrometer. Transmission electron microscope (TEM) measurement was performed on a JEOL JEM-1400 transmission electron microscope operating at 120 kV. Atomic force microscope (AFM) characterization was performed on an SPA 300HV instrument with an SPI 3800 controller (Seiko Instruments). A silicon micro cantilever (spring constant 2 N m^{-1} and resonance frequency ca. 300 kHz, Olympus Co., Japan) with an etched conical tip was used for the scan. Thickness of films was measured with an XP-plus Stylus Profilometer. Two-dimensional grazing-incidence wide angle X-ray scattering (2D-GIWAXS) was measured at Shanghai Synchrotron Radiation Facility (SSRF) on beamline BL14B1 (λ = 0.124 nm) with a MarCCD area detector at incidence angle of 0.16°. Samples were prepared on Si substrates using identical blend solutions as those used in devices.

The J–V plots of the devices were measured using a Keithley 2400 source meter under 100 mW cm^{-2} AM 1.5G simulated solar light illumination provided by a XES-40S2-CE Class Solar Simulator (Japan, SAN-EI Electric Co., Ltd.) or under indoor light. The emission spectra and light intensity of the LED light sources were measured by a Fiber Optics Spectrometer (Maya2000 Pro, Ocean Optics). The test devices were placed directly below the center of the light source. We calibrate the light intensity and spectrum of measuring points before testing, and for modules, the light intensity of the device center is calibrated. The EQE spectra were measured using a Solar Cell Spectral Response Measurement System QE-R3011 (Enlitech Co., Ltd.) under the short-circuit condition at a chopping frequency of 165 Hz.

SCLC mobility measurements

The hole-only device structure is ITO/PEDOT:PSS (40 nm)/active layer/MoO_3 (10 nm)/Al (100 nm) and the electron-only device structure is ITO/PEIE (10 nm)/active layer/Ca (20 nm)/Al (100 nm). J–V plots in the range of 0–10 V of the devices were measured using a Keithley 2400 source meter. The hole and electron mobilities were estimated using space-charge-limited current (SCLC) method by fitting the J–V plots near quadratic region according to the modified Mott-Gurney equation:

$$J = \frac{9}{8}\varepsilon_r\varepsilon_0\mu\frac{V^2}{L^3}\exp\left(0.89\beta\frac{\sqrt{V}}{\sqrt{L}}\right)$$

Where J is the current density, ε_0 is permittivity of free space, ε_r is the relative permittivity (assumed to be 3), μ is the zero-field mobility, V is the potential across the device ($V = V_{applied} - V_{bi} - V_{series}$), L is the thickness of active layer, and β is the field-activation factor. The series and contact resistance of the device (10–20 Ω) were measured using blank device of ITO/PEDOT:PSS/MoO_3/Al or ITO/PEIE/Ca/Al.

Coherence length calculation

The information about the size of crystalline grains is contained in the width of the diffraction peaks, and it can be expressed by the Scherrer equation, $CL = 2\pi K/(\Delta q)$, which gives an approximation of the grain size CL. where K is a shape factor (typically 0.9) and Δq is the full width at half-maximum of a diffraction peak (Rivnay et al., 2012; Song et al., 2018).

Fabrication of small-area photovoltaic devices

The all-polymer photovoltaic devices were fabricated with the configuration of ITO/PEDOT:PSS/active layer/LiF/Al. ITO glass substrates were cleaned by sequential ultrasonication in detergent, deionized water, acetone, and isopropyl alcohol, followed by dried at 120°C for 45 min and treated with UV-ozone for

20 min. Then the PEDOT:PSS solution (Clevios VP AI 4083 from H. C. Starck Inc.) was spin-coated on the ITO glass substrates at 5000 rpm for 40 s to give a thickness of 40 nm. Then the substrates were baked at 120°C for 20 min and then transferred to a nitrogen-filled glovebox. CD1 and PBN-21 were dissolved in tetrahydrofuran (THF) with a weight ratio of 1:1 and a total concentration of 8 mg mL^{-1}. Then the active layer was made by either spin-coated at 3000 rpm for 1 min, blade-coated at shearing rate of 35 mm/s with the substrate temperature of 25°C or 55°C. The gap between the substrate and blade is 500 μm. Then the active layers were annealed at 80°C for 10 min. The thickness of the spin-coated film is 90 nm and the thickness of the two blade coated film is 110 nm. Finally, 0.5 nm LiF and 100 nm Al were thermally deposited onto the active layer through a shadow mask in a vacuum chamber with a pressure under 2×10^{-4} Pa. The active area of the device was 0.08 cm^2.

Fabrication of all-polymer photovoltaic modules

The ITO-glass substrate with the size of 5 cm × 5 cm was patterned by laser etching. The module was composed of five single cells in series with an effective area of 10 cm^2 and a geometric filling factor (GFF) of 40%. The device structure of each single cell is ITO/PEDOT:PSS/active layer/LiF/Al and the active layer was blade coated at 55°C. After the preparation of the active layer, the dead area between five connected cells were scraped off.

QUANTIFICATION AND STATISTICAL ANALYSIS

To compare the device performance changes, the photovoltaic parameters reported in this work are the average values of multiple devices under the same conditions.